

Photon flux requirements for extreme ultraviolet reticle imaging in the 22- and 16-nm nodes

Daniel T. Wintz
Kenneth A. Goldberg
Iacopo Mochi

Lawrence Berkeley National Laboratory
Center for X-Ray Optics
Berkeley, California 94720
E-mail: KAGoldberg@lbl.gov

Sungmin Huh

Samsung
San # 16, Banweol-Dong
Hwaseong-City
Gyeonggi-Do, Korea, 445-701

Abstract. Extreme UV (EUV)-wavelength actinic microscopy yields detailed information about EUV mask patterns, architectures, defects, and the performance of defect repair strategies without the complications of photoresist imaging. To understand the pattern measurement limits of EUV mask microscopy, we investigate the effects of shot noise on aerial image linewidth measurements in the 22- and 16-nm lithography generations. Using a simple model we probe the influence of photon shot noise on measured, apparent line roughness, and find general flux density requirements independent of the specific EUV microscope configurations. Analysis reveals the trade-offs between photon energy density, effective pixel dimension on the CCD, and image log slope (ILS). We find that shot-noise-induced linewidth roughness (LWR) varies inversely with the square root of the photon energy density and is proportional to the magnification ratio. While high magnification is necessary for adequate spatial resolution, for a given flux density, higher magnification ratios have diminishing benefits. We find that to achieve an LWR (3σ) value of 5% of linewidth for dense, 88-nm mask features with a 2.52 normalized ILS value (image log-slope, ILS, equal to $28.6/\mu\text{m}$) and 13.5-nm effective pixel width ($1000 \times$ magnification ratio), a peak photon flux of approximately 1400 photons/pixel per exposure is required. © 2010 Society of Photo-Optical Instrumentation Engineers. [DOI: 10.1117/1.3491512]

Subject terms: extreme ultraviolet lithography; extreme ultraviolet; linewidth roughness; actinic mask inspection; reticle; imaging.

Paper 10051SSPR received Apr. 12, 2010; revised manuscript received Jul. 22, 2010; accepted for publication Jul. 22, 2010; published online Nov. 29, 2010.

1 Introduction

Lithographic imaging requirements include exceptionally tight specifications on the linewidth roughness (LWR) (i.e., width variation) and defects in printed lines. These specifications limit roughness to a small fraction of the printed linewidth and consequently shrink with every generation, making them more difficult to achieve. Target specifications on printed lines are typically defined as LWR (3σ) values not exceeding 5% of the half-pitch or critical dimension (CD) value. For the 22- and 16-nm nodes, these 3σ values at 5% linewidth are therefore only 1.1 and 0.8 nm, respectively. Furthermore, isolated defects may be defined as any printable, local pattern-edge perturbation that exceeds a given fraction of the linewidth.

Accurately detecting defects and roughness, prior to printing in photoresist, is essential to the success of every lithography node, and mask-imaging microscopy provides that essential quantitative feedback. Industry concern over the current unavailability of commercial extreme UV (EUV) mask inspection tools focuses increased attention on working prototypes such as the SEMATECH Berkeley Actinic Inspection Tool,^{1,2} (AIT) an EUV-wavelength, Fresnel zone-plate microscope operating at Lawrence Berkeley National Laboratory, and on plans for future tools. One consistent thread in these discussions is the limited brightness and high cost of suitable or available EUV sources. Along with these concerns is a great desire to create high-throughput mask-

imaging tools. Since photon flux is the foundation of high throughput, understanding the minimum flux requirements for accurate line imaging is an important step in the design and creation of new capabilities.

1.1 LWR

Many factors contribute to the roughness of printed lines, including inherent mask pattern roughness, mid-spatial-frequency optical aberrations in the projection imaging system, especially the physical granularity (i.e. local inhomogeneity), and other limitations of photoresist materials.^{3–5} Furthermore, recent investigations have revealed that EUV lithography faces a unique challenge from multilayer phase roughness, which modifies the light field reflected from the mask surface and contributes⁶ to printed LWR.

Owing to the highly wavelength specific reflective response of EUV masks, multilayer phase roughness can be difficult to detect during mask inspection. Mask inspection techniques that do not use EUV light—scanning-electron microscopy (SEM), deep-ultraviolet (DUV) microscopy, atomic-force microscopy (AFM), and others—have not demonstrated predictive capabilities for observed LWR. AFM, for example, can detect roughness in the mask surface height profile; the correlation of observed height variations with the magnitude of the phase roughness is a subject of ongoing investigation. Yet even if precise correlation were established, AFM is very slow and cannot be used in a practical way to predict local linewidth variations across large mask areas. SEM clearly reveals the borders of absorber patterns,

but cannot predict the EUV optical properties of arbitrary surface defects, or the local reflected phase variations from the multilayer. DUV microscopy, which is currently used as a high-throughput mask inspection technique, may never reach the nanometer-scale resolution required to see relevant pattern roughnesses. In addition, because DUV light penetrates only the top few layers of an EUV multilayer,⁷ it cannot predict the EUV reflected phase variations in all cases.

For ideal, smooth lines, the observed roughness level is strongly dependent on the integrated photon flux per image pixel. In this paper, we demonstrate that actinic (EUV wavelength) mask imaging can reveal roughness in the aerial image with the required levels of sensitivity and accuracy, provided that there is sufficient photon flux to overcome shot noise. Modeling photon shot noise in a direct EUV mask-imaging configuration with ideal line intensity profiles enables us to predict the minimum photon flux requirements of EUV mask inspection tools and to understand the dependencies on magnification, image log slope (ILS), and linewidth. This modeling is similar to studies of shot noise in photoresist,⁸ but here is applied to direct EUV imaging with a charge-coupled device (CCD) camera. We compare the flux requirements predicted by modeling to the imaging parameters of the AIT. An example of line images recorded with the AIT using different exposure times is also given.

1.2 EUV Images from the AIT

The AIT records high-quality EUV mask images and is now used in a wide variety of mask measurements, including mask-blank^{9,10} and pattern defect characterizations,¹¹ defect repair studies,¹² and the analysis of line properties.¹³

Flux-dependent line roughness effects are readily apparent in images collected with the AIT. Operating near the 13.4-nm wavelength, the AIT currently uses a CCD camera with 13.5- μm square pixels and a 907 \times magnification ratio, giving an effective pixel size of 14.9 nm, in mask units. Flux levels measured on the CCD camera vary with mask and pattern properties; exposure times are adjusted to achieve 750 to 1000 photons per CCD pixel in the bright regions.

Figure 1 shows an example with four different exposure times. A 2- μm -long detail region is extracted from an image of 250-nm lines (mask dimensions). In Fig. 1(a), an inherent and reproducible pattern of intensity variation is readily apparent as a primary source of LWR in these lines. Closer inspection reveals the roughness arising from shot noise, especially in the 10-s image. A SEM micrograph of the identical mask region is shown in Fig. 1(b) for direct comparison. While the SEM does reveal some level of pattern roughness, the origin and magnitude of the aerial image intensity variations cannot be attributed to variations observed in the SEM.

1.3 LWR Measurement and Modeling

With real, EUV microscope images, recorded with a CCD camera, line properties can be extracted from close examination of the 2-D measured intensity profiles. Some line properties, such as linewidth, ILS, and contrast can be calculated by averaging along the direction of the lines; this

averaging can significantly increase the SNR, incorporating the contributions of many times more detected photons in the measurement. However, LWR must be computed in a different manner. In one methodology, a line's width, at the threshold intensity level, is computed separately, by interpolation or fitting, in each perpendicular row of an image detail. The array of width measurements can then be analyzed to reveal the average linewidth, the standard deviation, and the spatial frequency spectrum. (LWR is taken to mean three times the standard deviation, 3σ .) This line-by-line analysis relies on individual pixel intensity measurements, and thereby makes the measurement vulnerable to shot noise; especially in the presence of insufficient or borderline flux levels.

In practice, the LWR measured in an EUV microscope is a statistical combination of the systematic, inherent roughness in the aerial image (from many sources) and the random noise sources, typically dominated by photon shot noise. Our goal in this analysis is to isolate the effects of shot noise. Therefore, we model ideal, smooth lines and measure only the roughness induced by noise.

Ideally, in the absence of noise, the linewidth is determined by the intensity at the threshold-crossing positions, independent of any other properties of the line profile or intensity contrast. When noise is introduced, the linewidth varies in a manner that depends on the intensity slope at the threshold-crossing positions. Our understanding of this effect follows from conventional descriptions of the exposure latitude,³ described in Sec. 2.

For these reasons, we neglect the specific details of the aerial image line profile, which arise from the complex interaction of illumination, coherence, numerical aperture (NA), aperture shape, and mask properties, as well as mask pattern shadowing, horizontal-vertical (HV) bias, and illumination angle of incidence, in favor of a sinusoidal line profile model. While the sinusoidal model does not capture the details of a physical line's aerial image it is a reasonable simplification of the smoothly varying profile across the threshold-crossing intensity level.

2 Modeling LWR Dependence on Measurement Parameters

It is instructive to begin the investigation with an analytic description of the influence of shot noise on the threshold position. In practice, we sample the intensity at discrete pixel locations and interpolate to find the threshold-crossing position. Here, we simplify the description by concentrating on a single pixel that is assumed to be centered at the threshold-crossing location. We find that this model conservatively over-predicts the LWR by roughly 20% in typical conditions.

2.1 Simple Model of LWR Dependence on ILS and Aerial Image Flux Density

A simple model for the measured LWR induced by photon shot noise can be derived from the local intensity slope measured at the threshold-crossing position where the line edge is defined. A measured position x responds to local intensity changes as

$$\Delta x \approx \frac{\Delta I}{dI/dx}. \quad (1)$$

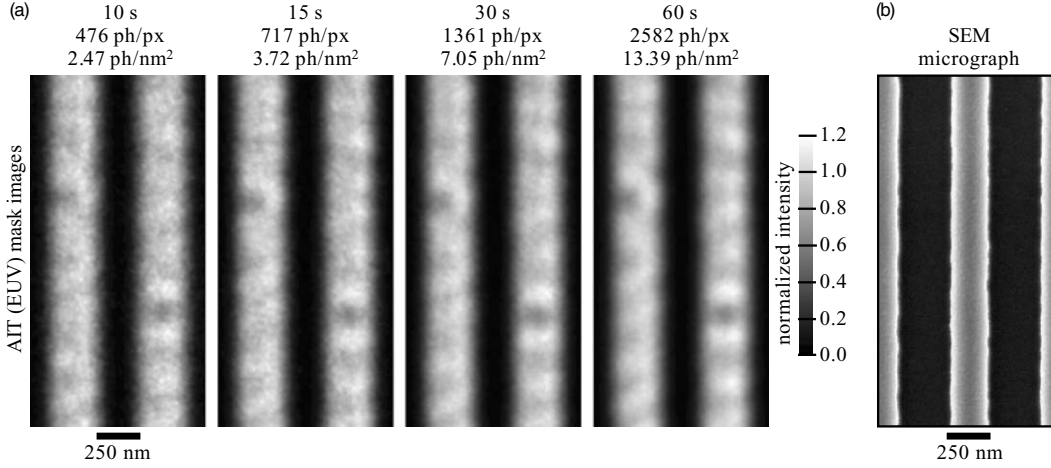


Fig. 1 Comparison of EUV aerial image measurements with an SEM micrograph from the identical region of the mask: (a) increasing exposure time and photon energy density, noticeably smooths the line images, with a clear improvement occurring between 2.47 to 13.39 photons/nm²; (b) SEM reveals pattern roughness, but cannot predict the features that produce the static pattern of intensity variation observed in these lines.

It is convenient to introduce the expression for the ILS, defined at the threshold-crossing position x_T :

$$\text{ILS} \equiv \left. \frac{d \ln I}{dx} \right|_{x_T} = \frac{1}{I_T} \left. \frac{dI}{dx} \right|_{x_T}. \quad (2)$$

For simplicity, we assume that the line's intensity profile is symmetric, with equal slope magnitude on both sides. The intensity threshold level is I_T , and the derivative is evaluated at the threshold position. Equation (1) can be written with ILS:

$$\Delta x = \frac{1}{\text{ILS}} \frac{\Delta I}{I_T}. \quad (3)$$

When intensity is measured with a given exposure time on a square pixel of effective width p (measured in mask units), the average number of photons detected at the intensity threshold level I_T can be defined as N_T . Here, N_T is the product of the effective pixel area p^2 and the (time integrated) energy density, measured in photons, n_T (in photons per square nanometer). Thus,

$$N_T = p^2 n_T. \quad (4)$$

For realistic line profiles, the peak intensity level may be 2 to 4 times higher than the threshold level, depending on the pattern and optical system dependent aerial image properties. Note that the magnification ratio m links the effective pixel size p and the physical size of the detector pixels, p_{CCD} : $m = p_{\text{CCD}}/p$, and is of the order of 1000.

The one-sided line-edge position root mean square due to shot noise follows from the normalized uncertainty in the intensity variation

$$\sigma_{x_T} = \frac{1}{\text{ILS} \sqrt{N_T}}. \quad (5)$$

The measured linewidth w is the distance between the left- and right-side threshold positions, represented as the difference between the two x positions. Therefore, considering that the two sides of the line are detected by separate detector pixels with uncorrelated responses, the linewidth un-

certainty is $\sqrt{2}$ larger. This gives us a general expression for the measured line width uncertainty. Note that LWR is $3\sigma_w$.

$$\sigma_w = \frac{\sqrt{2}}{\text{ILS} \sqrt{N_T}}, \quad (6a)$$

$$\text{LWR} = \frac{3\sqrt{2}}{\text{ILS} \sqrt{N_T}}. \quad (6b)$$

To isolate the role of the effective pixel size p , it is convenient to express the LWR from Eq. (6b) using the time-integrated flux density from Eq. (4).

$$\text{LWR} = \frac{3\sqrt{2}}{\text{ILS} p \sqrt{n_T}}. \quad (7)$$

For fixed photon flux density, the LWR therefore increases in proportion to the magnification ratio,

$$\text{LWR} = \frac{3\sqrt{2}m}{\text{ILS} p_{\text{CCD}} \sqrt{n_T}}. \quad (8)$$

2.2 Sinusoidal Model for the Aerial Image

For a dense-line mask pattern near the spatial resolution limit of the objective lens in an EUV microscope, the intensity profiles of the projected image at the CCD plane can be described with a smoothly varying, periodic intensity function. In a coherent, aberration-free optical system, where the pupil serves as a filter in the angular-frequency domain, only the zeroth and first diffracted orders from a uniform line pattern are transmitted to reach the image plane. When partially coherent illumination is used, the aerial image profile depends on the illumination in a complex way, typically smoothing small ripples and sharp features.

Only the threshold-crossing regions of the line profile contribute to the line edge positions. For the purposes of this study, we use a simple, sinusoidal model of the aerial image intensity profile. The sinusoidal model, while missing the details of a physical line shape, provides a smooth function that is easy to analyze and interpret.

We can apply the general expressions of Eq. (7) to a sinusoidal intensity profile model, written with the linewidth w , contrast c , and the intensity at threshold I_T as

$$I(x) = I_T \left[1 + c \cos\left(\frac{\pi x}{w}\right) \right]. \quad (9)$$

With this sinusoidal intensity pattern, the ILS value follows the line contrast in a predictable way. We evaluate the derivative and the photon flux at the threshold position

$$\text{ILS} = \frac{c\pi}{w}. \quad (10)$$

Here, it is important to recognize that the contrast parameter c depends on the shape of the line profile, and is therefore not universal. The modeled LWR dependence is more accurately described by its relationship with the ILS [or normalized ILS (NILS)] parameter than with the contrast. Where appropriate, we have included both parameters for convenience.

Finally, we reach the predicted LWR dependence on linewidth, contrast, CCD effective pixel size, and the energy density at the threshold energy, measured in photons.

$$\text{LWR} = \frac{3\sqrt{2}w}{\pi cp\sqrt{n_T}}. \quad (11)$$

It may be more convenient to refer to the incident photon energy density n_i rather than the energy density at threshold. These two energy densities are related by a constant: $n_i = n_T(1 + c)$.

$$\text{LWR} = \frac{3[2(1 + c)]^{1/2}w}{\pi cp\sqrt{n_i}}. \quad (12)$$

As with Eq. (8), we can represent the explicit dependence of LWR on the magnification ratio:

$$\text{LWR} = \frac{3[2(1 + c)]^{1/2}wm}{\pi cp_{\text{CCD}}\sqrt{n_i}}. \quad (13)$$

Equations (9) to (13) refer only to the specific case of sinusoidal line profiles, where the contrast parameter c is a convenient descriptor. For arbitrary line intensity profiles, the more general equations of Sec. 2.1 must be used.

3 Simulation of Shot Noise and Minimum Flux Requirements

To probe the effects of shot-noise-induced LWR in EUV microscope imaging, we modeled noise on CCD images, and quantified the minimum flux requirements for EUV mask inspection tools. Our goal is to achieve LWR magnitudes below 10 or 5% of the linewidth (also referred to a CD). In all cases, we assume a square, CCD pixel width of 13.5 μm , matching the CCD currently used in the AIT. The effective pixel widths, 6.5 to 20 nm, are calculated from the various magnification ratios we consider. Furthermore, the photon energy densities quoted refer to detected photons (independent of detector quantum efficiency), scaled to mask dimensions for convenience.

In the line profile calculations, we limit our noise considerations to photon shot noise, neglecting contributions from camera dark current, ambient stray light, etc. The photon

shot noise is added to calculated line profiles using the pseudorandom number generator from MATLAB[®]'s Statistics Toolbox[™], following the Poisson distribution, and the pixel intensity values are discretized to represent the number of detected photons. Each pixel of the simulated image has an error with a standard deviation $\sigma = p\sqrt{n_T}$.

Note that at a 13.5-nm wavelength, one EUV photon carries 91.84 eV or 1.47×10^{-17} J, and 1 μW is 6.80×10^{10} photons/s.

3.1 Modeling the Ideal Aerial Image Intensity Function

Following Eq. (9), we use a sinusoidal model of the aerial image intensity distribution from a pattern of parallel lines, near the optical system's resolution limit. The local intensity $I(x)$ varies with the lateral position x , N_T is the average number of photons detected per pixel at 1:1 line-to-space ratio threshold, the intensity contrast is c , the CCD effective pixel size (in mask units) is p , and the ideal linewidth is w . Since we do not intentionally control the relative position of the line pattern on the CCD pixel grid, we include an additional grid-position offset parameter, δ .

$$I(x) = I_T \left\{ 1 + c \cos\left[\frac{\pi(x + \delta)}{w}\right] \right\}. \quad (14)$$

Figure 2 contains a series of simulated mask line images with varying photon flux densities to illustrate how photon shot noise creates a dependence of measured line roughness on the number of photons per pixel. The gray-scale intensity in each image is scaled to the brightest pixel value.

From the CCD pixel array, intensity measurements are assigned to points separated by the pixel spacing p . Despite the discrete sampling, linear interpolation enables us to determine the threshold position to a fraction of the pixel spacing.

3.2 Systematic Difference between the Analytic and the Numerical Model

A systematic difference between the simple, analytic model and the numerical analysis arises from the way that the threshold position is determined in practice. In the numerical analysis, as for experimental data, each threshold-crossing position is calculated from at least two adjacent intensity measurements: one on either side of the threshold. In contrast, the analytic model described in Sec. 2 is based on a simplification that the intensity slope and the intensity uncertainty are known precisely at the threshold-crossing position—a position that is not knowable in advance. In this way, comparing a single, ideal, known point, to an interpolation between two intensity measurements, the calculated threshold position uncertainty becomes somewhat lower than that predicted analytically. The threshold position is calculated from a weighted average using two, independent intensity measurements (i.e., by interpolation), rather than from one single measurement. This difference gives rise to the systematic LWR overestimation in the simple models.

The shot-noise-dependent position uncertainty that arises from the interpolation equation is much more difficult to generalize or write in a closed form, given the arbitrary location of the threshold with respect to the adjacent pixels,

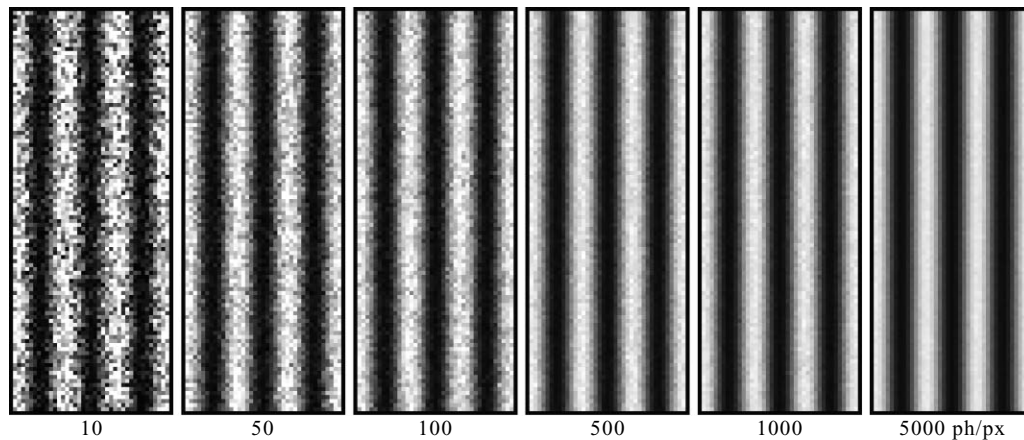


Fig. 2 Simulated mask images with varying photon flux densities show how photon shot noise creates a sensitive dependence of measured line roughness on the number of photons per pixel. Shown are 88-nm lines (half-pitch) recorded with an effective pixel size of 13.5 nm on the mask and 80% aerial image contrast.

and the independent intensity uncertainties assigned to each pixel. This is the most significant advantage of the simple model.

3.3 Simulation Method

Simulation begins with the construction of an ideal CCD image, following Eq. (14), with a given N_T value. Following Poisson statistics pixel by pixel, we add shot noise to the ideal image and calculate the LWR properties, as described in Sec. 1.3. A MATLABTM pseudorandom number generator, *poissrnd*, which follows the Poisson distribution, is used.

Our studies show that the apparent LWR does have a small position dependence, typically below 0.6 nm, that is periodic with the CCD pixel size. We attribute this to small variations in the local intensity slope across the pixels where the threshold intensity levels are measured. To remove the position bias from our calculations, for each set of calculation parameters, we average the results from 100 uniformly sampled δ values, from 0 to $0.99p$.

In each row of the simulated images (perpendicular to the line direction), we use linear interpolation to find the two positions where the intensity function crosses the threshold value. The local linewidth is calculated as the distance between the two threshold-crossing positions. A schematic of this procedure is shown in Fig. 3.

For each configuration of the imaging parameters, and the two different linewidths of interest (64- and 88-nm mask linewidths), LWR calculations were performed 10,000 times using model images with 2000 pixel rows per image. The results of our studies are shown in Fig. 4.

3.4 LWR Induced by Image Rotation

Due to the AIT's unusual rotation-translation ($x\theta$) mask stage, images are projected onto the CCD at arbitrary rotation angles. Therefore, we also investigated the measured-LWR dependence on image rotation, separate from the shot noise considerations. Briefly, our analysis showed that

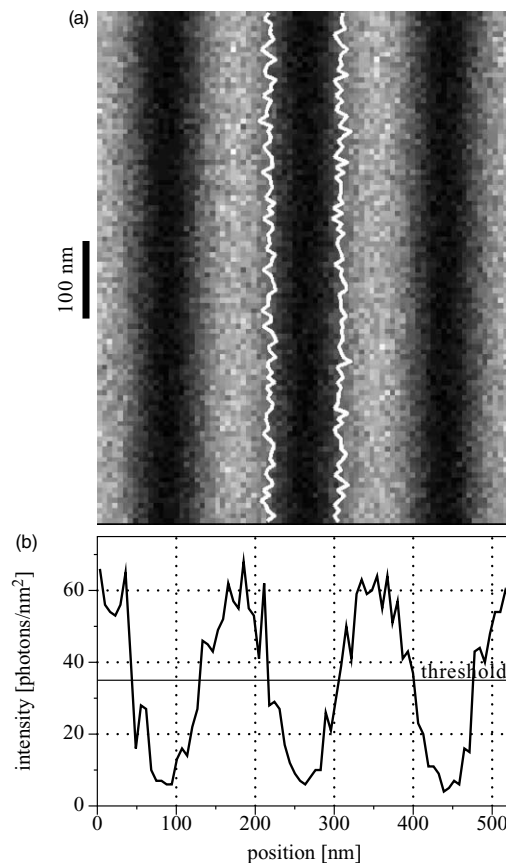


Fig. 3 (a) Detail from a simulated aerial image with shot noise, an effective pixel size of 6.5 nm (mask units), $39.3/\mu\text{m}$ ILS (80% contrast), 88-nm linewidth, and 35 photons/pixel ($0.83 \text{ photons}/\text{nm}^2$) at threshold. The jagged white lines show the threshold-crossing positions and thus the variation in linewidth caused by shot noise. Threshold positions are calculated with interpolation. (b) A cross section from the uppermost row in the aerial image detail. The solid horizontal line shows the position of the line edge at the threshold intensity level. The detail in this example will have high apparent roughness from inadequate mask illumination.

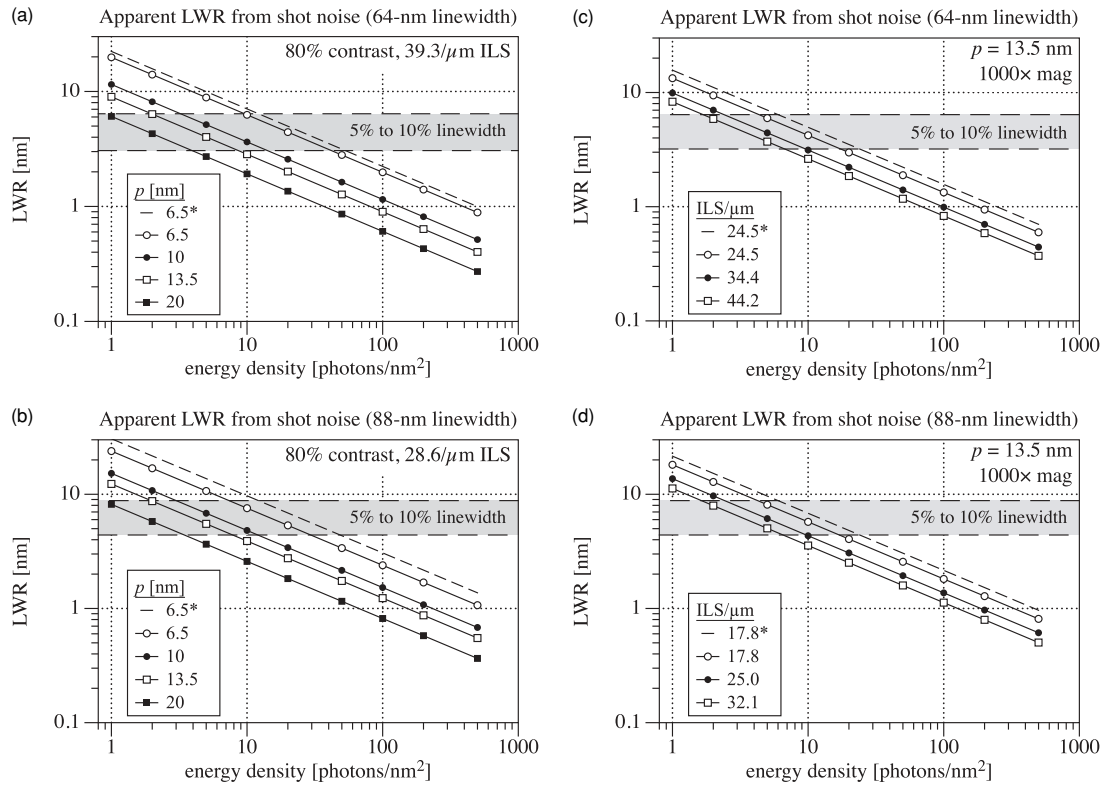


Fig. 4 Calculated LWR, in mask units, for different effective pixel sizes (i.e., physical size scaled by the magnification ratio), NILS and ILS values, aerial image contrast, and photon densities, with a sinusoidal aerial image. In each graph, the gray band shows a 5 to 10% linewidth range for LWR values. (a) and (b) LWR for 64- and 88-nm linewidths with 39.3 and 28.6/μm ILS values, respectively. The theory values (dashed line, values indicated by *) are shown for one effective pixel size. (c) and (d) Calculated LWR for four different contrast values at a 13.5-nm effective pixel size. Theory curves are shown (dashed line, and contrast values indicated by *). In all cases, theory overestimates the detailed calculation by approximately 20%. Note that while the NILS and ILS values given here can be applied to arbitrary line-profile shapes, the specified contrast values apply only to sinusoidal profiles.

in the worst case, image rotation with a linear interpolation adds a spatially periodic linewidth variation that is typically not larger than 0.5 nm (3σ), for the range of magnification and linewidth values already described. This

effect is significantly smaller than contributions from shot noise, and will likely not be an issue of concern for future EUV mask microscopes that use a linear xy mask stage (i.e. no mask rotation).

Table 1 Empirical calculation of the A values [Eq. (15)] from the simulated 64-nm lines.^a

ρ (nm)	Mag. ratio	Contrast	NILS	ILS (1/μm)	A	Photon density (photons/nm ²) for LWR = 10% CD	Photon density (photons/nm ²) for LWR = 5% CD	A (Theory)
6.5	2077	80%	2.52	39.3	19.81	9.58	38.32	22.30
10.0	1350	80%	2.52	39.3	11.51	3.23	12.94	14.50
13.5	1000	50%	1.57	24.5	13.34	4.34	17.38	15.68
13.5	1000	70%	2.20	34.4	9.91	2.40	9.59	11.93
13.5	1000	80%	2.52	39.3	8.99	1.97	7.89	10.74
13.5	1000	90%	2.83	44.2	8.30	1.68	6.73	9.81
13.5	1000	100%	3.14	49.1	7.67	1.44	5.75	9.05
20.0	675	80%	2.52	39.3	6.07	0.90	3.60	7.25

^aThe parameter A (found by a linear fit to the simulated data) is the LWR ($3\sigma_w$) when the photon energy density is 1 photon/nm². Theory values follow Eq. (13).

Table 2 Empirical calculation of the A values [Eq. (15)] from the simulated 88-nm lines.

ρ (nm)	Mag. ratio	Contrast	NILS	ILS (1/ μm)	A	Photon density (photons/nm ²) for LWR = 10% CD	Photon density (photons/nm ²) for LWR = 5% CD	A (Theory)
6.5	2077	80%	2.52	28.6	23.89	7.36	29.46	30.66
10.0	1350	80%	2.52	28.6	15.25	3.00	12.01	19.93
13.5	1000	50%	1.58	17.9	18.13	4.24	16.98	21.56
13.5	1000	70%	2.20	25.0	13.70	2.42	9.69	16.40
13.5	1000	80%	2.52	28.6	12.32	1.96	7.84	14.76
13.5	1000	90%	2.82	32.1	11.25	1.63	6.54	13.48
13.5	1000	100%	2.26	35.7	10.40	1.40	5.89	12.45
20.0	675	80%	2.52	28.6	8.17	0.86	3.45	9.97

4 Empirical Fit to the Calculated LWR

The results of the simulations follow the dependencies predicted in the analytic model. Our simulation demonstrates a relationship of the form given in Eq. (11). Again, a physical CCD square pixel width of 13.5 μm is assumed, with different magnification ratios providing various effective pixel sizes, in mask units.

$$\text{LWR} = \frac{A}{\sqrt{n_i}}. \quad (15)$$

The constant coefficient A depends on the measurement parameters, and n_i is the (time integrated) detected incident photon density, scaled to mask units, measured by the CCD detector. Tables 1 and 2 list the empirically fit values of A for the specific cases presented here. From multiple simulations, we estimate a relative uncertainty in A values of 1%.

5 Conclusion

The prediction of shot noise on all-EUV actinic microscope imaging for the 16- and 22-nm nodes enables us to determine minimum detected photon flux requirements as a function of linewidth, microscope image magnification, and line ILS. The analytic model given in Eqs. (12) and (13) predicts the dependences of LWR on various parameters and provides a conservative estimate of the LWR, typically 10 to 20% above the simulated values. Measured LWR varies inversely with the square root of the photon energy density. Furthermore, LWR varies inversely with ILS. These results are merely a restatement of the expected conclusions. Clearly, the more photons the better, and the sharper is the aerial image, the smaller will be the measured LWR.

Our sinusoidal aerial image model reveals that across the majority of experimentally relevant cases studied, typical (time integrated) photon energy density requirements are 5 to 20 photons/nm² to achieve noise-added LWR levels below 5 to 10% CD. We also find that when the photon density drops below approximately 0.2 photons/nm², at a 13.5-nm effective pixel size, shot noise may render LWR measurements impossible. Configurations with different effective pixel sizes cross that critical threshold at levels close to that value.

The model also demonstrates the trade-offs inherent in the design of an EUV mask-imaging microscope. High magnification is necessary for clear imaging of small features, and the resolution must be high enough to oversample the mask features by a comfortable margin. However, for a given photon energy density, we find that measured LWR is inversely proportional to the magnification ratio. This arises from the strong dependence of LWR on the photon energy density. At higher magnifications, the energy density at the CCD plane drops as the square of the magnification. Thus, any gains that may come from a more densely sampled aerial image are outweighed by the loss of light.

At this time, for the 22- and 16-nm lithography nodes, we believe that reasonable effective pixel sizes (mask units) range from 5 to 20 nm. Modern EUV-direct-detection CCD cameras have pixels sizes close to 13 μm , so reasonable magnification ratios are in the approximate range of 700 to 2700 at this time. Without advances in detector technology, higher magnification ratios will be necessary with decreasing linewidths. However, the penalty paid in flux and the drive for short exposure times (and thus high measurement throughput) pushes designs toward the lowest acceptable magnification ratio.

Line measurement and LWR measurement are 1-D and 2-D problems, respectively. More challenging 2-D measurements, and the subject of ongoing research, are the photon density requirements for precise 2-D feature measurement, such as OPC (optical proximity correction) and corner rounding. Accurate and rapid characterization of these aerial image properties is a necessary role for EUV actinic patterned mask inspection.

Acknowledgments

We wish to acknowledge the support of SEMATECH project leader Sungmin (Sean) Huh, and insightful feedback from Patrick Naulleau (Lawrence Berkeley National Laboratory) and Chris Mack (Lithoguru). This work was supported by SEMATECH, through the U.S. Department of Energy under Contract No. DE-AC02-05CH11231.

References

1. K. A. Goldberg, P. Naulleau, I. Mochi, E. H. Anderson, S. B. Rekawa, C. D. Kemp, R. F. Gunion, H.-S. Han, and S. Huh, "Actinic extreme ultraviolet mask inspection beyond 0.25 numerical aperture," *J. Vac. Sci. Technol. B* **26**(6), 2220–2224 (2008).
2. K. A. Goldberg, I. Mochi, P. P. Naulleau, H. Han, and S. Huh, "Benchmarking EUV mask inspection beyond 0.25 NA," *Proc. SPIE* **7122**, 71222E-1–8 (2008).
3. C. A. Mack, "Understanding focus effects in submicron optical lithography," *Proc. SPIE* **922**, 135–148 (1988).
4. J. Shin, G. Han, Y. Ma, K. Moloni, and F. Cerrina, "Resist line edge roughness and aerial image contrast," *J. Vac. Sci. Technol. B* **19**(6), 2890–2895 (2001).
5. A. Saeki, T. Kozawa, S. Tagawa, and H. B. Cao, "Line edge roughness of a latent image in post-optical lithography," *Nanotechnology* **17**, 1543–1546 (2006).
6. P. P. Naulleau, D. Niakoula, and G. Zhang, "System-level line-edge roughness limits in extreme ultraviolet lithography," *J. Vac. Sci. Technol. B* **26**(4), 1289–1293 (2008).
7. A. Barty, K. A. Goldberg, P. Kearney, S. B. Rekawa, B. LaFontaine, O. Wood II, J. S. Taylor, and H.-S. Han, "Multilayer defects nucleated by substrate pits: a comparison of actinic inspection and non-actinic inspection techniques," *Proc. SPIE* **6349**, 63492M (2006).
8. P. Naulleau and J. Cain, "Experimental and model-based study of the robustness of line-edge roughness metric extraction in the presence of noise," *J. Vac. Sci. Technol. B* **25**(5), 1647–1657 (2007).
9. S. Huh, P. Kearney, S. Wurm, F. Goodwin, K. Goldberg, I. Mochi, and E. Gullikson, "Mask defect verification using actinic inspection and defect mitigation technology," *Proc. SPIE* **7271**, 72713J-1–9 (2009).
10. S. Huh, L. Ren, D. Chan, S. Wurm, K. Goldberg, I. Mochi, T. Nakajima, M. Kishimoto, B. Ahn, I. Kang, J. Park, K. Cho, S.-I. Han, and T. Laursen, "A study of defects on EUV masks using blank inspection, patterned mask inspection, and wafer inspection," *Proc. SPIE* **7636**, 76360K-1–7 (2010).
11. S. Huh, P. Kearney, S. Wurm, F. Goodwin, H. Han, K. Goldberg, I. Mochi, and E. Gullikson, "EUV actinic defect inspection and defect printability at the sub-32 nm half-pitch," *Proc. SPIE* **7470**, 74700Y-1–7 (2009).
12. H. Han, H. Seo, K. Goldberg, H. Kim, B. Ahn, I. Kang, W. Cho, S. Lee, G. Kim, D. Kim, S. Kim, and H. Cho, "Characterization of EUV mask defects: printability, inspectability and repair," in *Proc. EUVL Symp. 2008* (2008).
13. K. A. Goldberg, I. Mochi, P. Naulleau, T. Liang, P.-Y. Yang, and S. Huh, "EUV pattern defect detection sensitivity based on aerial image linewidth measurements," *J. Vac. Sci. Technol. B* **27**(6), 2916–2921 (2009).



Daniel T. Wintz graduated with a BS degree in engineering physics from the University of California, Berkeley, in 2009. As an undergraduate, he was a technical staff intern at The Aerospace Corporation for three summers working on remote sensing, characterization, and analysis. Since graduation, he has been with Lawrence Berkeley National Laboratory examining the effects of shot noise in extreme UV (EUV) mask inspection and new ways to align zoneplate

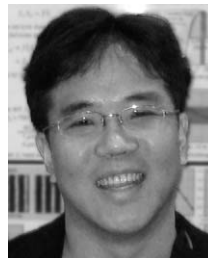
microscope systems. He is currently a graduate student in applied physics at Harvard University.



Kenneth A. Goldberg is the deputy director of Lawrence Berkeley National Laboratory's Center for X-Ray Optics. He specializes in the development of technologies for extreme UV (EUV) and soft x-ray wavelengths, including lithography, mask inspection, and wavefront-measuring interferometry. Dr. Goldberg is the principal investigator of the SEMATECH Berkeley Actinic Inspection Tool (AIT), an EUV reticle-imaging microscope, and he is a cocreator of the SEMATECH Berkeley MicroExposure Tool (MET). Dr. Goldberg received an AB degree in physics and applied math and a PhD degree in physics from the University of California, Berkeley. He has authored and coauthored over 160 publications, and has received 12 patents.



Iacopo Mochi graduated in physics at the University of Florence, Italy, in 2001, and received his PhD degree with a thesis on the optical design of a fluorescence LIDAR for the remote sensing of the sea surface in 2005. For 3 years he was with the Italian National Institute for Astrophysics (INAF), working on the development of astronomical instrumentation. Since 2008 Dr. Mochi has been with Lawrence Berkeley National Laboratory working first as a postdoctoral scholar and currently as a project scientist for the SEMATECH Berkeley Actinic Inspection Tool, and investigating various aspects of extreme UV (EUV) optics and mask inspection.



Sungmin Huh graduated in material science engineering from the Hanyang University, Korea, in 2002 and joined the Samsung Electronics. For 8 years he has been with the photomask team in the semiconductor division. In 2009, he joined SEMATECH for 2 years as an assignee for Samsung Electronics, where he was the project manager of the SEMATECH Berkeley Actinic Inspection Tool (AIT) and led defect printability studies of extreme UV (EUV) masks.